

Response of convectively coupled Kelvin waves to surface temperature forcing in aquaplanet simulations

Mu-Ting Chien¹ and Daehyun Kim²

¹University of Washington

²Seoul National University

April 16, 2024

Abstract

This study investigates changes in the propagation and maintenance of convectively coupled Kelvin waves (KWs) in response to surface warming. We use a set of three aquaplanet simulations made with the Community Atmospheric Model version 6 by varying the sea surface temperature boundary conditions, representing the current climate, a warmer (+4K), and a cooler (-4K) climate. Results show that KWs accelerate at the rate of about 7.1%/K and their amplitudes decrease by 4.7%/K. The dampening of KWs with warming is found to be associated with a weakening of the internal thermodynamic feedback between diabatic heating and temperature anomalies that generates KW eddy available potential energy (EAPE). The phase speed of KWs closely matches that of the second baroclinic mode KW in -4K, while the phase speed of KWs is approximately that of the first baroclinic mode KW in +4K. Meanwhile, the coupling between the two baroclinic modes weakens with warming. We hypothesize that in -4K, as the first and second modes are strongly coupled, KWs destabilize by positive EAPE generation within the second mode, and they propagate slower following the second mode KW phase speed. In +4K, as the first and second modes decouple, KWs are damped by negative EAPE generation within the first mode, and they propagate faster following the first mode KW phase speed.

1
2
3
4
5
6
7
8
9
10
11
12
13
14
15
16
17

Response of convectively coupled Kelvin waves to surface temperature forcing in aquaplanet simulations

Mu-Ting Chien¹ and Daehyun Kim^{1,2*}

¹Department of Atmospheric Sciences, University of Washington

²School of Earth and Environmental Sciences, Seoul National University, South Korea

*Corresponding author: Daehyun Kim (daehyun@snu.ac.kr)

Key Points:

- Convectively coupled Kelvin waves (KWs) weaken and accelerate as the surface warms.
- Internal thermodynamic feedback is the dominant KW maintenance mechanism in our simulations.
- The weakening and acceleration of KWs with warming are associated with KWs transitioning from the second mode dynamics in -4K to the first mode dynamics in +4K.

Abstract

19 This study investigates changes in the propagation and maintenance of convectively
20 coupled Kelvin waves (KW) in response to surface warming. We use a set of three aquaplanet
21 simulations made with the Community Atmospheric Model version 6 by varying the sea surface
22 temperature boundary conditions, representing the current climate, a warmer (+4K), and a cooler
23 (-4K) climate. Results show that KWs accelerate at the rate of about 7.1%/K and their
24 amplitudes decrease by 4.7%/K. The dampening of KWs with warming is found to be associated
25 with a weakening of the internal thermodynamic feedback between diabatic heating and
26 temperature anomalies that generates KW eddy available potential energy (EAPE). The phase
27 speed of KWs closely matches that of the second baroclinic mode KW in -4K, while the phase
28 speed of KWs is approximately that of the first baroclinic mode KW in +4K. Meanwhile, the
29 coupling between the two baroclinic modes weakens with warming. We hypothesize that in -4K,
30 as the first and second modes are strongly coupled, KWs destabilize by positive EAPE
31 generation within the second mode, and they propagate slower following the second mode KW
32 phase speed. In +4K, as the first and second modes decouple, KWs are damped by negative
33 EAPE generation within the first mode, and they propagate faster following the first mode KW
34 phase speed.

35

Plain Language Summary

37 Convectively coupled Kelvin waves (KW) regulate the variability of tropical
38 precipitation on the subseasonal timescale. The change of KWs with surface warming is studied
39 using three ocean-only global simulations with different sea surface temperatures. We find that
40 KWs are weaker, and they propagate faster in a warmer climate. The results further suggest that
41 the changes in the amplitude and phase speed of KWs with warming can be explained by the
42 those in the thermodynamic structure of KWs.

43

44 **1 Introduction**

45 Convectively coupled Kelvin waves (KWs) are a dominant force in tropical subseasonal
46 precipitation variability (Murata et al. 2006; Wang and Fu 2007; Sinclaire et al. 2015; Chen et al.
47 2019; Latos et al. 2021). These waves exert significant influence on global weather extremes and
48 climate variability across multiple scales (Flatau et al. 2003; Bessafi and Wheeler 2006; Straub et
49 al. 2006; Roundy 2008; Lawton and Majumdar 2023; Cheng et al. 2023). The profound impacts
50 of KWs on such a broad spectrum of climatic phenomena underscore the necessity to understand
51 their dynamics, particularly as the climate continues to warm.

52 While many studies have studied the changes in the Madden-Julian Oscillation (MJO) in a
53 warmer climate (e.g., Adames et al. 2017a,b; Rushley et al. 2019; Bui and Maloney 2020),
54 research into the response of convectively coupled equatorial waves (CCEWs) to similar
55 conditions has been relatively scarce. Bartana et al. (2022) stands as an exception in this regard,
56 utilizing global climate model (GCM) simulations from the sixth phase of the Coupled Model
57 Intercomparison Project (CMIP6) to investigate CCEWs in a warming climate. Their findings
58 indicate an intensification and acceleration of KWs with warming, as evidenced by increased
59 KW variance in outgoing longwave radiation and upper tropospheric zonal wind, alongside an
60 increase in the equivalent depth of the strongest KW signal strength. While they documented the
61 changes in KW characteristics as the climate warms, however, the mechanisms behind the
62 changes in KWs in a warmer climate remain unclear.

63 Previous observational and modeling studies have suggested two mechanisms for KW
64 maintenance: the internal thermodynamic feedback and the external momentum forcing exerted
65 by midlatitude Rossby waves. The internal feedback mechanism posits that KWs grow through
66 the interaction between diabatic heating and temperature anomalies, which amplifies the KW
67 eddy available potential energy (EAPE) (Lindzen 1974; Emanuel 1987; Mapes 2000; Straub and
68 Kiladis 2003a; Khouider and Majda 2006; Raymond and Fuchs 2007; Kuang 2008; Chien and
69 Kim 2023). While earlier simple models attributed this growth to deep convective clouds within
70 the first baroclinic mode (e.g., Lindzen 1974; Emanuel 1987; Raymond and Fuchs 2007), more
71 recent observational and modeling evidence highlighted the significant role of stratiform cloud
72 processes within the second baroclinic mode (e.g., Mapes 2000; Straub and Kiladis 2003a;
73 Khouider and Mada 2006; Kuang 2008; Chien and Kim 2023). Chien and Kim (2023), through a
74 thorough analysis of KW EAPE growth rates in multiple reanalysis products, underscored the

75 dominance of the second baroclinic mode in the generation of KW EAPE. Their finding is
76 consistent with the results of an earlier observational study which hypothesized that the presence
77 of the second mode contributes to large KW EAPE generation in the upper troposphere (Straub
78 and Kiladis 2003a).

79 In the meantime, studies have suggested that midlatitude Rossby waves, through a resonance
80 mechanism involving momentum flux convergence in the subtropics and KW wind anomalies,
81 could remotely amplify KW eddy kinetic energy (EKE) (Hoskins and Yang 2000; Straub and
82 Kiladis 2003b; Tulich and Kiladis 2021; Cheng et al. 2022). When the midlatitude waves
83 approach the critical latitude in the subtropics, which is the location where the background
84 westerly wind has the same speed as the phase speed of the westward-propagating midlatitude
85 waves, the wave propagation is blocked. This leads to the momentum flux convergence and
86 divergence around the critical latitude, which acts as a transient forcing of the zonal wind
87 (Randel and Held 1991). When the phase speed of such momentum forcing is the same as the
88 phase speed of the KWs, the momentum forcing can resonate with KW zonal wind structures and
89 thereby amplify the KWs. This remote influence of midlatitude waves is suggested to be
90 important for KW maintenance in observations (Cheng et al. 2022) and aquaplanet simulations
91 (Tulich and Kiladis 2021).

92 In a warmer climate, changes in the mean state may affect how convection and wave are
93 coupled in the tropics, as well as the strength of midlatitude wave influence, which may change
94 the relative importance of the internal and external mechanisms. In the present study, we
95 investigate the relative importance of the two maintenance mechanisms across different climates
96 to better understand changes in KW amplitude as the surface warms.

97 Regarding KW propagation, KWs propagate eastward at a speed of approximately 10-20 m/s
98 in the current climate (Kiladis et al. 2009). This range of KW phase speeds is understood as the
99 result of the dry Kelvin waves being slowed down due to the coupling with moist convection.
100 Previous studies argued that the observed KW phase speed can be explained as either the first
101 baroclinic mode dry Kelvin wave phase speed (~ 49 m/s) substantially reduced by convective
102 coupling (e.g., Lindzen 1974; Emanuel 1987; Raymond and Fuchs 2007), or the second
103 baroclinic mode dry Kelvin wave phase speed (~ 23 m/s) that is slightly reduced by convective
104 coupling (e.g., Mapes 2000; Kuang 2008); debate persists over which offers a more accurate
105 explanation of the observed KW phase speed. In a warmer climate, while changes in the mean

106 state and convective coupling of KWs potentially affect KW propagation, the specific effects of
107 individual factors on KW phase speed with warming are yet to be determined.

108 Aquaplanet simulations—conducted on a water-covered Earth with idealized, time-
109 independent sea surface temperatures (SST)—serve as our investigative tool. These simulations
110 offer a simplified yet potent setting to explore the maintenance and propagation mechanisms of
111 KWs, free from the confounding factors of seasonality and regionality (Straub and Kiladis 2002;
112 Roundy and Frank 2004; Yang et al. 2007; Dias and Pauluis 2011; Yasunaga 2011; Wang and
113 Chen 2016). Aquaplanet simulations have been used to study the characteristics of CCEWs,
114 including KWs, and their interactions with the basic states (e.g., Leroux et al. 2016; Tulich and
115 Kiladis 2021; Rios-Berrios et al. 2023). For example, Leroux et al. (2016) found that warm pool
116 favors the development of MJO-like variability. Specifically targeting the maintenance of KWs
117 and MJO, Tulich and Kiladis (2021) tested the importance of midlatitude waves and the effect of
118 basic state zonal wind.

119 In the current study, we conduct and analyze aquaplanet simulations to investigate the
120 changes in KWs with surface warming. While doing so, we quantify the relative roles of the
121 internal thermodynamic feedback and the external forcing in maintaining KWs. We also
122 investigate factors affecting KW propagation changes in different climates. The subsequent
123 sections of this manuscript are organized as follows: Section 2 describes the design of our
124 aquaplanet simulations and the methodologies employed for calculating the generation of KW
125 EAPE and EKE, as well as the theoretical KW phase speed. Section 3 examines the changes in
126 KW characteristics with warming, including the relative importance of the internal and external
127 mechanisms of KW maintenance and the KW propagation mechanisms. A hypothesis on why
128 KW amplitude and phase speed change with warming is proposed in the end. Finally, Section 4
129 consolidates our conclusions and summarizes the main findings of our study.

130 **2 Simulations and Methods**

131 **2.1 Aquaplanet Simulations**

132 Our study utilizes the sixth version of the Community Atmosphere Model (CAM6) to
133 conduct aquaplanet simulations. The simulations operate on a horizontal grid resolution of 1.9°
134 latitude by 2.5° longitude, encompassing 32 vertical levels. A brief description of the model
135 dynamics and parameterization schemes used in these simulations is provided in Table 1. We run

136 the model over a twelve-year period, allocating the initial two years to the spin-up phase—
 137 allowing the model to reach an equilibrium state—and dedicating the remaining ten years to the
 138 data analysis phase, during which we collect 3-hourly output. We verify that equilibrium was
 139 reached after the two-year integration period (now shown).

140

141 **Table 1.** Model dynamics and parameterization schemes used in our simulations.

Model component	Reference
Dynamical core	Finite Volume (Lin 2004)
Radiation	Rapid Radiative Transfer Model (RTMG, Iacono et al. 2008)
Deep convection	Zhang and McFarlane (1995)
Boundary layer turbulence, shallow convection, and cloud macrophysics	Cloud Layers Unified by Binormals (CLUBB, Golaz et al. 2002; Bogenschutz et al. 2013)
Cloud microphysics	Advanced Two-Moment Prognostic Cloud Microphysics (MG2, Gettelman and Morrison 2015)

142

143 To assess the influence of surface temperatures on KWs, we design three experiments
 144 using prescribed sea surface temperature (SST) conditions that are zonally uniform and time-
 145 invariant. Following the “Qobs” profile in Neale and Hoskins (2000), the meridional profile of
 146 SST in the control simulation (CTL) is designed as follows:

$$SST(\phi) = \begin{cases} 27 \times \left[1 - \frac{1}{2} \times \sin^2\left(\frac{\pi\phi}{120}\right) - \frac{1}{2} \times \sin^4\left(\frac{\pi\phi}{120}\right) \right], & |\phi| \leq 60^\circ \\ 0, & \textit{otherwise} \end{cases} \quad (1)$$

147 , where ϕ denotes latitude. The SST boundary conditions for the other two experiments, named
 148 +4K and -4K, are set by uniformly increasing and decreasing the SST globally by 4K,
 149 respectively, relative to the SST in the CTL experiment. The time-averaged zonal mean

150 temperature and circulation for each simulation are shown in Figure 1, and the time-averaged
 151 zonal mean precipitation and precipitable water are shown in Figure 2.

152 2.2 KW meridional projection

153 To derive the characteristics of KWs from our simulation data, we first isolate anomalies
 154 for each field variable by subtracting the slowly varying climatological mean state. This process
 155 involves removing both the time-averaged mean and any variabilities with a period longer than
 156 10 days, using a low-pass filter. The choice of a 10-day threshold is justified by the temporal
 157 scale of KWs in our simulations, which are typically shorter than this period.

158 We then focus on the tropical region, specifically between 10°S and 10°N, to examine the
 159 anomalies of precipitation, zonal wind, diabatic heating rate, and temperature. These anomalies
 160 are then projected onto the meridional structure characteristic of KWs—marked by a maximum
 161 at the equator and an exponential decay with latitude. The precise mathematical representation of
 162 this meridional structure is expressed as follows:

$$X_P = \int_{-\phi_{max}}^{\phi_{max}} X' \times w(\phi) \times e^{-\left(\frac{\phi}{\phi_0}\right)^2} d\phi, \quad (2)$$

163 where X represents field variables from aquaplanet simulations, including precipitation, zonal
 164 wind (u), diabatic heating (Q), and temperature (T), prime (') denotes anomalies, ϕ denotes
 165 latitude, ϕ_0 represents the meridional scale of KWs (9° as in Tulich and Kialdis 2021 and Cheng
 166 et al. 2022), $\phi_{max}=10^\circ$, and the weighting function w is defined as

$$w(\phi) = \begin{cases} 1, & |\phi| \leq 10^\circ \\ 0, & \text{otherwise} \end{cases}. \quad (3)$$

167 Note that in this paper, diabatic heating rate refers to temperature tendency due to moist
 168 processes. We confirm that the temperature tendency due to other processes (e.g., radiation)
 169 within KWs is negligible (only contributing 5% to the total temperature tendency) in our
 170 simulations.

171 In addition, to quantify the impact of midlatitude waves on KW zonal wind anomalies,
 172 we compute the zonal momentum flux convergence (F), which is instrumental in understanding
 173 the extent to which midlatitude dynamics contribute to the momentum budget of tropical Kelvin
 174 waves. F is defined by the following expression:

$$F = -\left(\frac{\partial u'u'}{\partial x} + \frac{\partial u'v'}{\partial y} + \frac{\partial u'\omega'}{\partial p}\right), \quad (4)$$

175 where v and ω represent meridional and vertical velocity in pressure coordinates, respectively.
 176 To isolate the momentum flux convergence attributable specifically to midlatitude Rossby waves
 177 and to exclude the influence of other tropical variabilities, we apply an extratropical filter to the
 178 zonal momentum flux convergence (F), following Tulich and Kiladis (2021) and Cheng et al.
 179 (2022):

$$F_P = \int_{-\phi_{max}}^{\phi_{max}} F' \times (1 - w(\phi)) \times e^{-\left(\frac{\phi}{\phi_0}\right)^2} d\phi, \quad (5)$$

180 where F_P represents the meridionally-projected zonal momentum flux convergence, ϕ and ϕ_0
 181 are the same as those in Eq. (2), and $\phi_{max} = 45^\circ$. The extratropical filter, denoted as $(1 -$
 182 $w(\phi))$, effectively diminishes the signal of tropical variability in the momentum flux
 183 convergence.

184 2.3 Space-time spectral analysis

185 We conduct a space-time spectral analysis on the equatorially symmetric component of
 186 precipitation anomalies. The raw power spectrum is normalized by the background spectrum,
 187 defined as the smoothed average of the raw spectrum. The resulting normalized power spectrum,
 188 which has often been referred to as the signal strength, is depicted in Figure 3.

189 We recognize that the spatial and temporal scale and the phase speed of KWs may exhibit
 190 variation across different climatic conditions. Consequently, instead of adopting the fixed KW
 191 band as defined by Wheeler and Kiladis (1999), we formulate our criteria to delineate the KW
 192 band. Specifically, we establish the KW band separately for each simulation by two distinct
 193 criteria: firstly, a high coherence squared between precipitation and column-integrated moisture;
 194 and secondly, a high coherence squared between precipitation and column-integrated
 195 temperature. These coherence relationships are visualized in Figure S1. These criteria are
 196 motivated by the understanding that KW precipitation is modulated by interactions with both
 197 atmospheric moisture and temperature, as suggested by recent findings (Weber et al. 2021). We
 198 posit that our tailored definition of the KW band is better suited for exploring the behavior of
 199 KWs under various climate scenarios.

200 To extract a time series representative of KW convective activity, we employ Fourier
201 space-time filtering on the meridionally projected precipitation anomalies. This filtering
202 technique selectively retains wave components falling within the KW band, which are outlined
203 by purple contours in Figure 3. Based on the lag regression of KW-filtered precipitation in Fig.
204 4, we estimate the average frequency, zonal wavenumber, and phase speed of KWs.

205 2.4. KW composite

206 Upon the derivation of the KW precipitation time series, we employ the compositing
207 approach of Nakamura and Takayabu (2022) to analyze the dynamical and thermodynamic
208 structure of KWs. Based on the value of the KW precipitation anomaly and its position relative
209 to the nearest local minimum and maximum, the KW phase is defined within the range of $-\pi$ to π
210 for each time and grid point. The most convectively active phase ($\pi/2$) is assigned to the local
211 maximum, while the most convectively inactive phase ($-\pi/2$) is assigned to the local minimum.
212 As in Nakamura and Takayabu (2022), we use local maxima and minima that are greater and
213 smaller than plus and minus one standard deviation ($\pm 1\sigma$) of the KW-filtered precipitation
214 anomalies in the entire dataset for each simulation, respectively. After determining the grid
215 points with the most enhanced or suppressed phase, the beginning and end of each KW event are
216 determined as the time when the KW-filtered precipitation anomalies reach an adjacent local
217 minimum, local maximum, or zero, whichever occurs closest to the peak. The phase for each
218 snapshot during a KW event is defined as the arcsine value of precipitation anomalies
219 normalized by the nearest peak value.

220 Subsequently, all projected fields (X_p and F_p in Section 2.2) are composited based on the
221 KW phase, resulting in KW composite fields (X_{KW}) as a function of the KW phase. By design,
222 the KW precipitation anomalies evolve sinusoidally (Fig. 5). The amplitude of a KW event is
223 quantified by averaging the absolute values of KW precipitation anomalies at the most enhanced
224 and the most suppressed phases within the event (Fig. 5).

225 2.5 Vertical mode decomposition

226 To delineate the contributions of the first and second baroclinic modes to the
227 maintenance and propagation of KWs, we perform an empirical vertical mode decomposition
228 analysis, as in Chien and Kim (2023). For Q and T, we derive the vertical modes through the

229 rotated EOF analysis of Q. The first two leading EOFs are rotated to ensure that their structures
 230 are physically consistent with our understanding of the first and second baroclinic modes. The
 231 rotation is done by applying a rotation matrix to the original EOFs:

$$\begin{bmatrix} EOF1_{rotated} \\ EOF2_{rotated} \end{bmatrix} = \begin{bmatrix} EOF1_{original} \\ EOF2_{original} \end{bmatrix} * \begin{bmatrix} \cos \theta & -\sin \theta \\ \sin \theta & \cos \theta \end{bmatrix}, \quad (7)$$

232 where θ is the rotation angle. The rotation angle is chosen to maximize the vertical integral of the
 233 rotated first EOF for each simulation, which enforces the first mode to have a single-signed vertical
 234 structure.

235 For dynamical consistency between Q and U, we obtain the vertical modes of U from that
 236 of Q. Specifically, we first divide the rotated EOFs of Q by the mean static stability at each level
 237 to obtain the corresponding vertical structure of vertical velocity in pressure coordinate (ω).
 238 Then, we differentiate the resulting vertical structure of ω with respect to pressure to obtain
 239 vertical modes of U. Note that we apply 10 passes of 1-2-1 filter to the vertical profiles of Q and
 240 U for their smoothness. The two vertical modes for Q and U are shown in Figs. 6, 7, and 8.

241

242 2.6 EAPE and EKE growth rates

243 To assess the role of internal thermodynamic feedback and external forcing on KW
 244 maintenance, we compute the growth rates of the eddy available potential energy (EAPE) and
 245 eddy kinetic energy (EKE) that are associated with the first and second baroclinic modes using
 246 KW composite fields (Fig. 9). The growth rate of EAPE indicates the strength of internal
 247 thermodynamic feedback, while the growth rate of EKE reflects that of external dynamic
 248 feedback. We calculate the growth rates based on updated methods originating from Chien and
 249 Kim (2023) and Tulich and Kiladis (2021).

250 The growth rate of EAPE, which is the rate of EAPE generation normalized by the total
 251 EAPE, is proportional to the covariance between diabatic heating rate and temperature
 252 anomalies:

$$\sigma_{EAPE_i} = \frac{\overline{Q_{l,KW} \times T_{l,KW}}}{0.5 \times \overline{T_{l,kw}^2}}, \quad i = 1 \text{ or } 2, \quad (8)$$

253 where subscript KW represents the KW composite fields, subscript i represents the vertical mode
 254 number. Similarly, the growth rate of EKE, which is the rate of EKE generation normalized by

255 the total EKE, is calculated based on the covariance between momentum flux convergence and
 256 zonal wind anomalies:

$$\sigma_{EKE_i} = \frac{\overline{F_{l,KW} \times U_{l,KW}}}{0.5 \times \overline{U_{l,KW}^2}}, \quad i = 1 \text{ or } 2. \quad (9)$$

257

258 2.7. KW propagation speed

259 Given the structural similarity between KWs and dry Kelvin waves, previous studies
 260 postulated that KWs are essentially manifestations of dry Kelvin waves influenced by moist
 261 convection, through modifying the adiabatic cooling and heating rates associated with the KW
 262 vertical motions (e.g., Kiladis et al. 2009). The adiabatic cooling and heating rates depend on the
 263 following physical parameters: the effective static stability, the tropospheric depth, and the
 264 vertical mode. In short, KWs propagate faster with increased effective static stability, increased
 265 tropospheric depth, and decreased vertical mode.

266 In a continuously stratified atmosphere, the phase speed of KWs can be determined as
 267 follows:

$$Cp = \sqrt{gh}, \quad (10)$$

268 where g is the gravitational acceleration constant, and h is the equivalent depth. The equivalent
 269 depth is defined as:

$$h = \frac{N^2(1 - \alpha)}{g \left(m^2 + \frac{1}{4Hs^2} \right)}, \quad (11)$$

270 where N represents dry static stability, α represents the reduction of dry static stability by
 271 diabatic heating, and m is the vertical wavenumber, defined as $m = 2\pi i / Lz$, with Lz being the
 272 tropospheric depth. The tropospheric depth Lz is estimated from the KW vertical structure of
 273 temperature. i denotes the vertical mode number defined in Section 2.5, and Hs is the scale
 274 height.

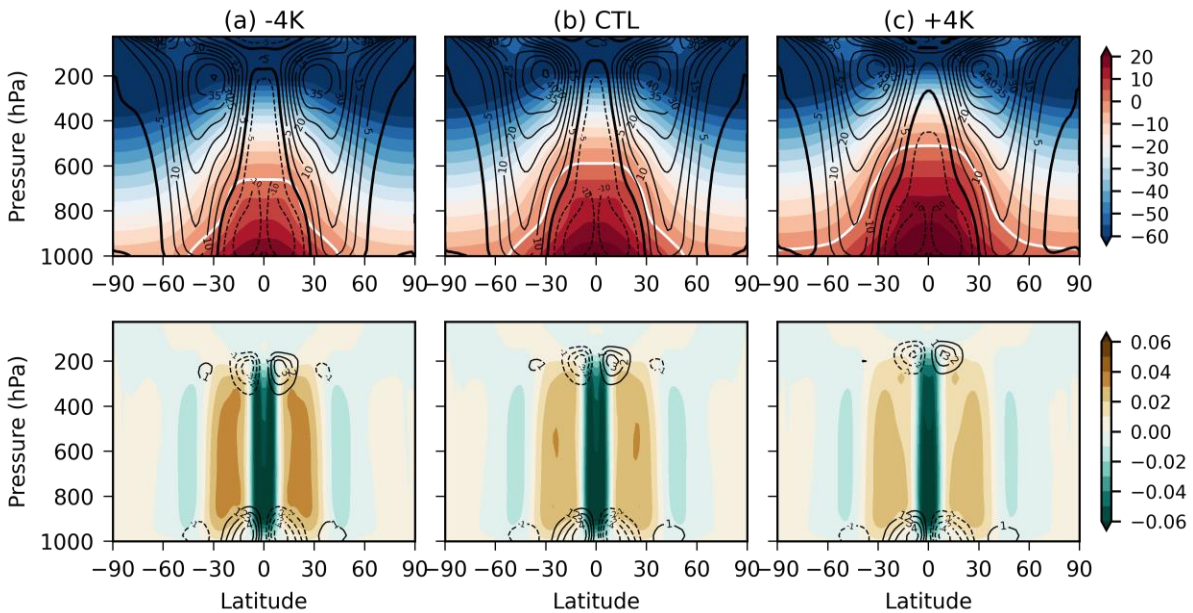
275 We calculate the theoretical phase speed of the first and second mode KW in each
 276 simulation (Fig. 10) based on Eqs (10) and (11) with the following estimation of the parameters:
 277 N is obtained from static stability profile weighted by each EOF mode, representing the static

278 stability that each vertical mode feels. The reduction factor α is estimated from the regression
 279 slope between the first two principal components of Q and the principal components of adiabatic
 280 cooling (ω^*S), where S represents the static stability in pressure coordinates. The principal
 281 components of ω^*S are obtained by projecting ω^*S onto vertical mode of Q .

282 3 Results

283 3.1 Changes in KW phase speed and amplitude

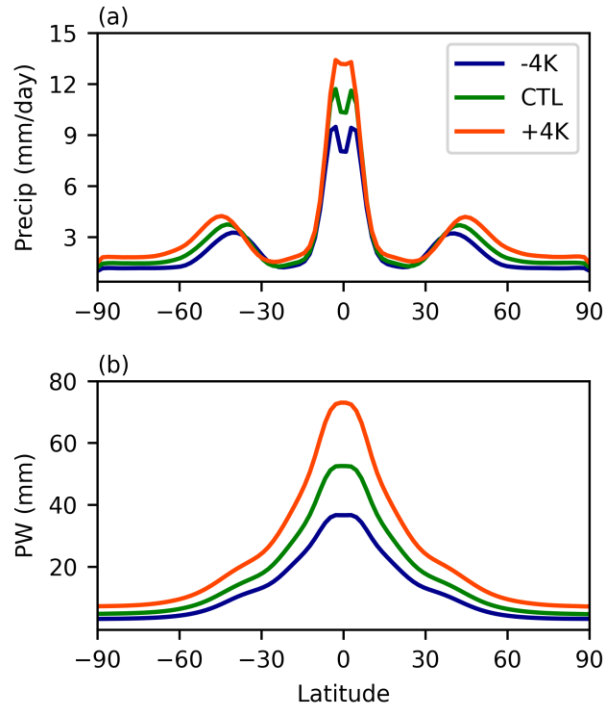
284 The time-averaged zonal mean circulation in our simulations shows robust Hadley
 285 circulation in the tropics and the subtropical jet stream (Fig. 1), mimicking the observed mean
 286 climate. As the surface warms, tropospheric temperature increases, and the Hadley circulation
 287 expands further to the upper troposphere. Meanwhile, the mean precipitable water and
 288 precipitation increases from -4K to +4K, especially in the tropics (Fig. 2).



289

290 **Figure 1.** Time-averaged zonal mean circulation and temperature in each simulation. Figures on
 291 the top row show temperature (shading, °C) and zonal wind (contours, m/s). The zero line for
 292 temperature (the melting level) is marked in white, and the zero line for zonal wind is marked in
 293 thick black line. Figures on the bottom row show vertical velocity (shading, Pa/s) and meridional
 294 velocity (contours, m/s).

295



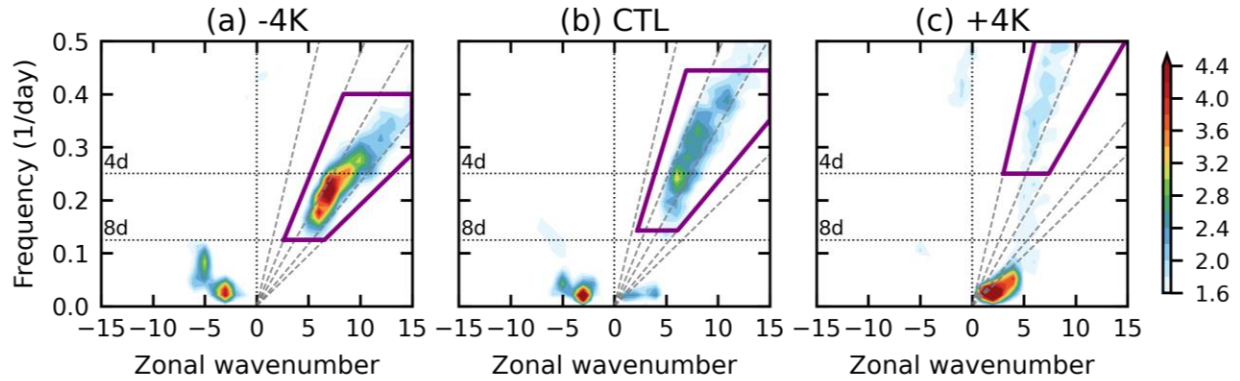
296

297 **Figure 2.** Time-averaged zonal mean (a) precipitation (mm/day) and (b) precipitable water (mm)
 298 in each simulation.

299

300 Despite the robust increase in the mean precipitation, different modes of subseasonal
 301 precipitation variabilities may respond differently to surface warming. To investigate the changes
 302 in subseasonal precipitation variabilities in wavenumber-frequency space, Figure 3 shows the
 303 normalized power spectrum of precipitation anomalies for the symmetric-to-the-equator
 304 component in -4K, CTL, and +4K simulations. As the surface warms, the low-frequency
 305 westward propagating signal (likely equatorial Rossby waves) weakens, and the low-frequency
 306 eastward propagating signal (likely MJO) strengthens. However, this is out of the scope of our
 307 paper as our focus is on KWs. KW bands are indicated in purple polygons with the boundaries in
 308 wavenumber-frequency space shown in Table 2. While KWs are pronounced in all simulations,
 309 the signal strength of precipitation within the KW band weakens from -4K to +4K. The raw
 310 power of precipitation within the KW band also weakens from -4K to +4K (not shown). In
 311 addition to the changes in KW amplitude, in a warmer climate, KWs appear in higher
 312 frequencies and align with the dispersive curve that corresponds to a higher equivalent depth,
 313 suggesting that KWs propagate faster.

314



315
316 **Figure 3.** Normalized power spectrum of the equatorially symmetric component of precipitation
317 anomalies over 15°S-15°N in each simulation. KW bands are indicated in purple polygons. The
318 grey slanted dashed lines represent different equivalent depths, which are 8m, 12m, 25m, 50m,
319 and 150m counterclockwise. The horizontal dotted lines indicate 4-day and 8-day.
320
321
322

Table 2. Boundaries of KW band in each simulation.

	-4K	CTL	+4K
Zonal wavenumber	1~15	1~15	1~15
Period (day)	2.5~8	2.25~7	2~4
Equivalent depth (m)	8~50	12~90	25~150

323
324 To better visualize the changes in KW characteristics, Figure 4 shows the lag regression
325 of KW precipitation on the Hovmoller diagram, represented by the reference point at 180°E.
326 Note that the result is consistent regardless of any other longitudes chosen as reference points.
327 Figure 4 shows that in a warmer climate, KWs are weaker and faster, and they appear in higher
328 frequencies, consistent with the findings in Fig. 3. To quantify the changes in zonal wavenumber,
329 frequency, and phase speed of KWs as the climate warms, we calculate the average zonal
330 wavenumber, frequency, and phase speed for each simulation, as shown in Table 3. KW
331 characteristics in Table 3 obtained from Figure 4 are consistent with the signal-strength-weighted
332 average over the wavenumber-frequency space within the KW band based on Fig. 3 (not shown).
333

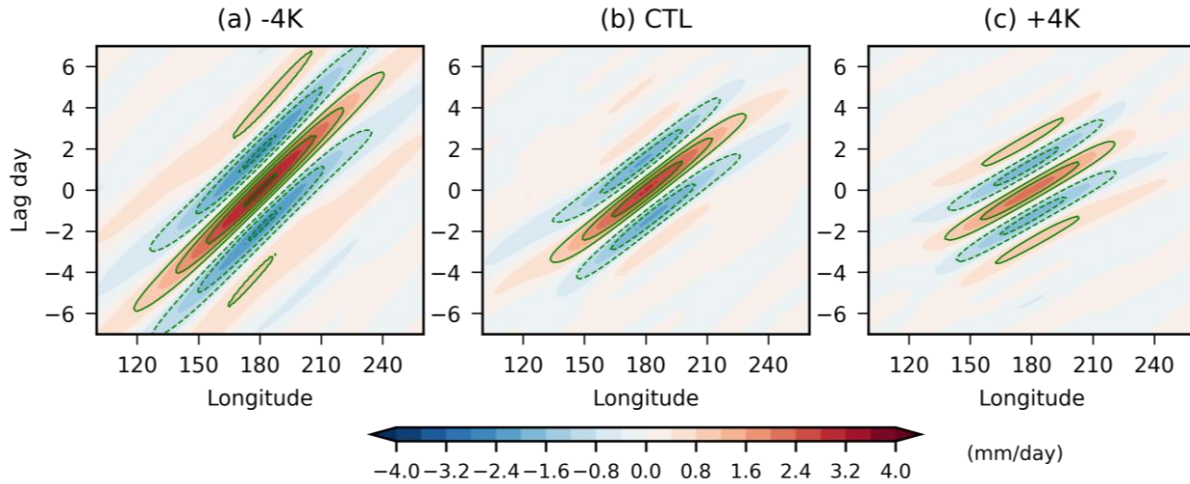


Figure 4. Lag regression of KW-filtered precipitation anomalies at each longitude upon those at the reference longitude (180°E) in each simulation. The contour interval is 0.8 mm/day . Solid lines represent positive values and dashed lines represent negative values. Zero lines are omitted.

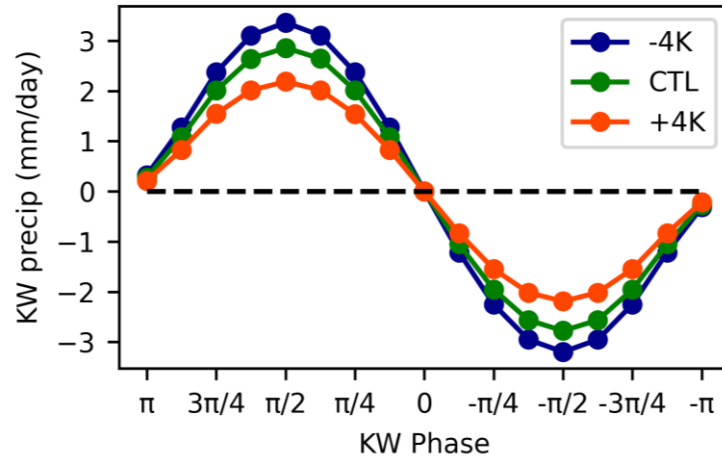
Table 3. KW characteristics in each simulation.

	-4K	CTL	+4K
Zonal wavenumber	9	9	8
Period (day)	3.75	3	2.5
Equivalent depth (m)	17.07	26.58	50.02
Phase speed (m/s)	12.94	16.14	22.14
Amplitude (mm/day)	3.26	2.85	2.19

Figure 5 shows the evolution of KW precipitation anomalies within the life cycle of KWs in each simulation. Note that the x-axis shows the KW phase, which can be considered as a time axis, with time increasing from the right to the left. Within the life cycle of KWs, precipitation anomalies present a sinusoidal evolution. Starting from the unperturbed phase ($-\pi$) when precipitation anomaly is zero, precipitation decreases until minimizing at the most suppressed phase ($-\pi/2$). Then, precipitation increases until maximizing at the most enhanced phase ($\pi/2$) and then returns to the unperturbed phase (π). While the sinusoidal evolution of precipitation anomalies exists in each simulation, KW amplitude decreases from 3.26 to 2.19 mm/day from -

350 4K to +4K (roughly $-4.7\%/K$). In Section 3.2 and 3.3, we focus on investigating why KWs are
 351 weaker and faster in a warmer climate.

352



353

354

355 **Figure 5.** KW phase composite of precipitation anomalies in each simulation.

356

357

3.2. Causes of the changes in KW amplitude

358

To investigate the cause of the changes in KW phase speed and amplitude, analyzing the
 359 role of the first and second baroclinic modes is necessary, as mentioned in Section 1. Figure 6a
 360 displays the vertical structure of diabatic heating and temperature anomalies of the first and
 361 second baroclinic modes. Figure 6b shows the corresponding zonal wind and momentum flux
 362 convergence anomalies.

363

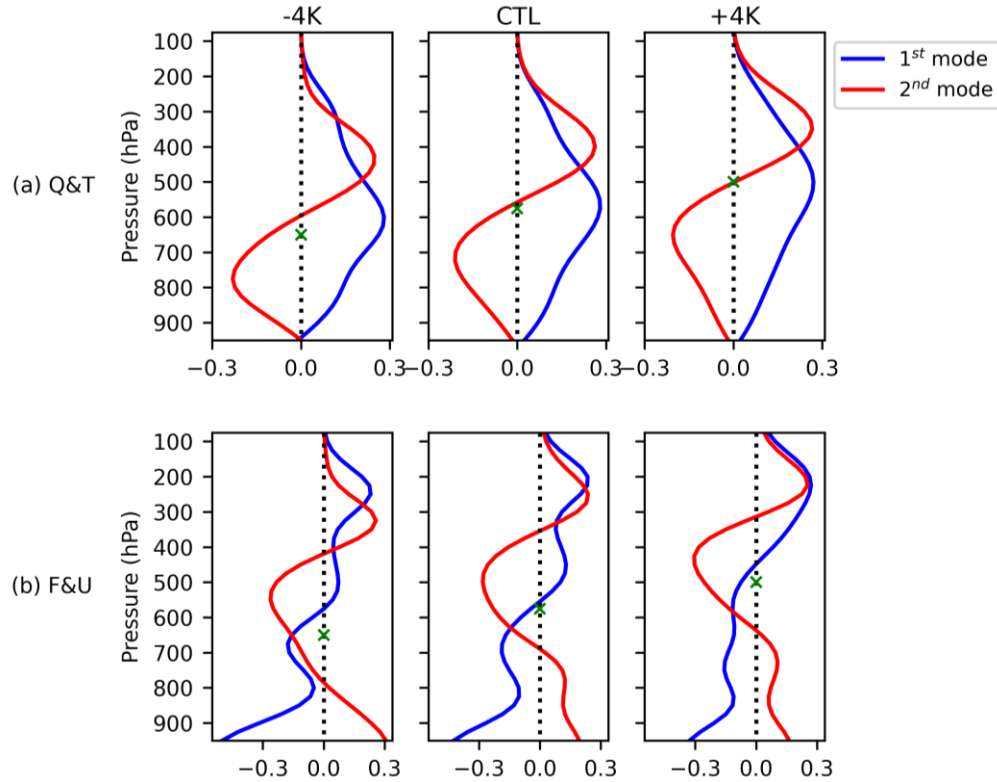


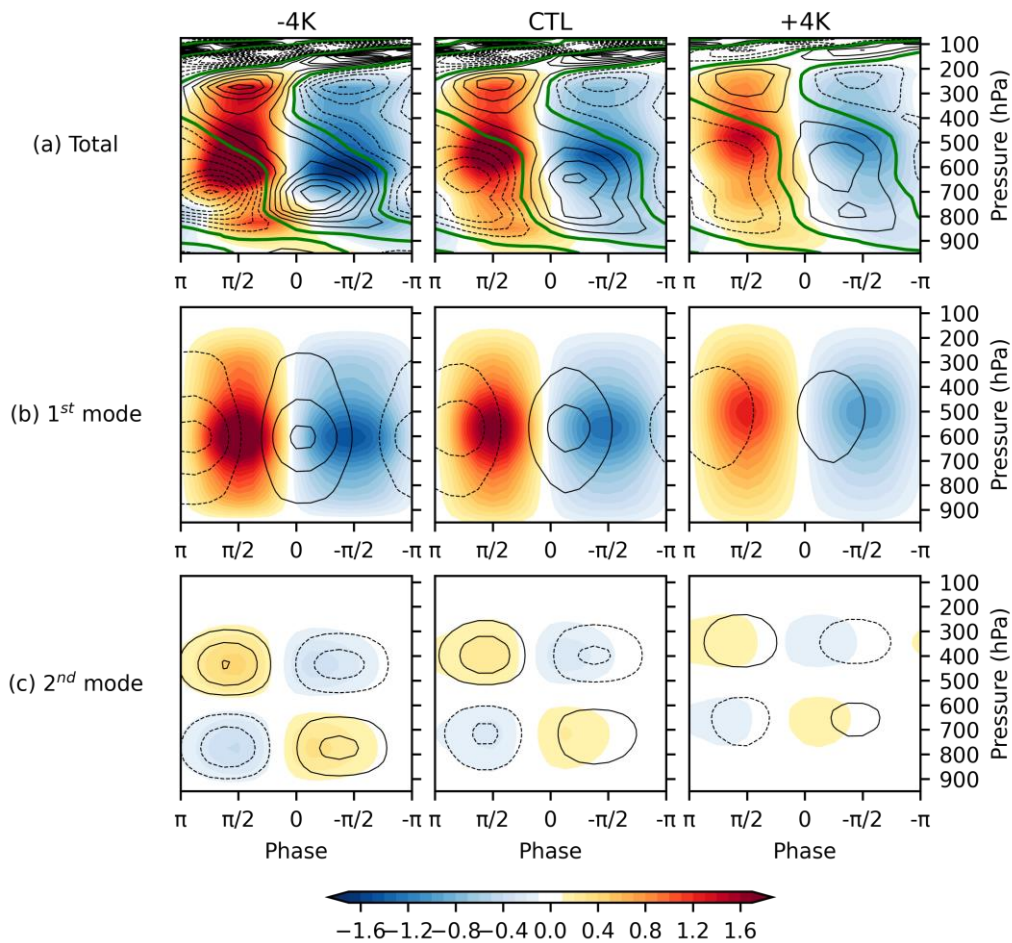
Figure 6. The vertical structure of the first (blue line) and second (red line) baroclinic modes of (a) diabatic heating and temperature, obtained from the EOF analysis of diabatic heating, and (b) zonal wind and momentum flux convergence, obtained from the vertical derivation of the EOF analysis of vertical pressure velocity in each simulation. Green crosses indicate the melting level, identified from the time-averaged zonal mean temperature profile in the tropics.

The two vertical modes in our simulations resemble the perceived structure of the first and second baroclinic modes. The first baroclinic structures represent the heating and circulation associated with deep convection. The first baroclinic heating structure presents a single signed heating over the entire tropics (blue lines in Fig. 6a) and the associated zonal wind structure exhibits opposite polarity between the upper and lower troposphere (blue lines in Fig. 6b). On the other hand, the second baroclinic structures represent the heating and circulation associated with stratiform and congestus processes. The second baroclinic heating structure is a dipole of heating and cooling (red lines in Fig. 6a), separated roughly by the melting level indicated with green crosses in Fig. 4a. The associated zonal wind structure (red lines in Fig. 6b) is characterized by three peaks in the upper-, mid-, and lower-troposphere.

From -4K to +4K, the structure of the first and second baroclinic modes expand further to the upper troposphere. The peak of the first baroclinic heating is shifted upward. Meanwhile, the most notable change in the second baroclinic heating structures is that the nodal point, which is

384 located close to the melting level (indicated in green crosses), is also shifted upward. Consistent
 385 with the upward expansion of the heating structures, the zonal wind structures also expand
 386 upward with warming.

387 To investigate the internal thermodynamic feedback in KW maintenance, Figure 7a shows
 388 the KW composite vertical structure of diabatic heating (shading) and temperature (contour)
 389 anomalies over the life cycle of KWs. In all simulations, negative heating anomalies peak when
 390 precipitation is most suppressed ($-\pi/2$), and, as time goes on, heating anomalies increase and
 391 maximize when precipitation anomalies are most enhanced ($+\pi/2$). From the most suppressed to
 392 the most enhanced phase, temperature anomalies within KWs evolve from cold-aloft-warm-
 393 below anomalies to warm-aloft-cold-below anomalies. The thermodynamic structure of KWs in
 394 our simulations is consistent with that in observations, reanalyses, and other model simulations
 395 (e.g., Kiladis et al. 2003; Tulich et al. 2007; Nakamura and Takayabu 2022; Chien and Kim
 396 2023).



398 **Figure 7.** Vertical mode decomposition of the KW phase composite diabatic heating (shading)
399 and temperature (contour) anomalies in each simulation: (a) the total anomalies, (b) the first
400 baroclinic mode obtained from the blue lines in Fig. 6a, and (c) the second baroclinic mode
401 obtained from the red lines in Fig. 6a. The green contour in (a) indicates the zero line for the
402 temperature anomalies. Solid contours represent positive values and dashed contours represent
403 negative values. The contour interval is 0.25 K.
404

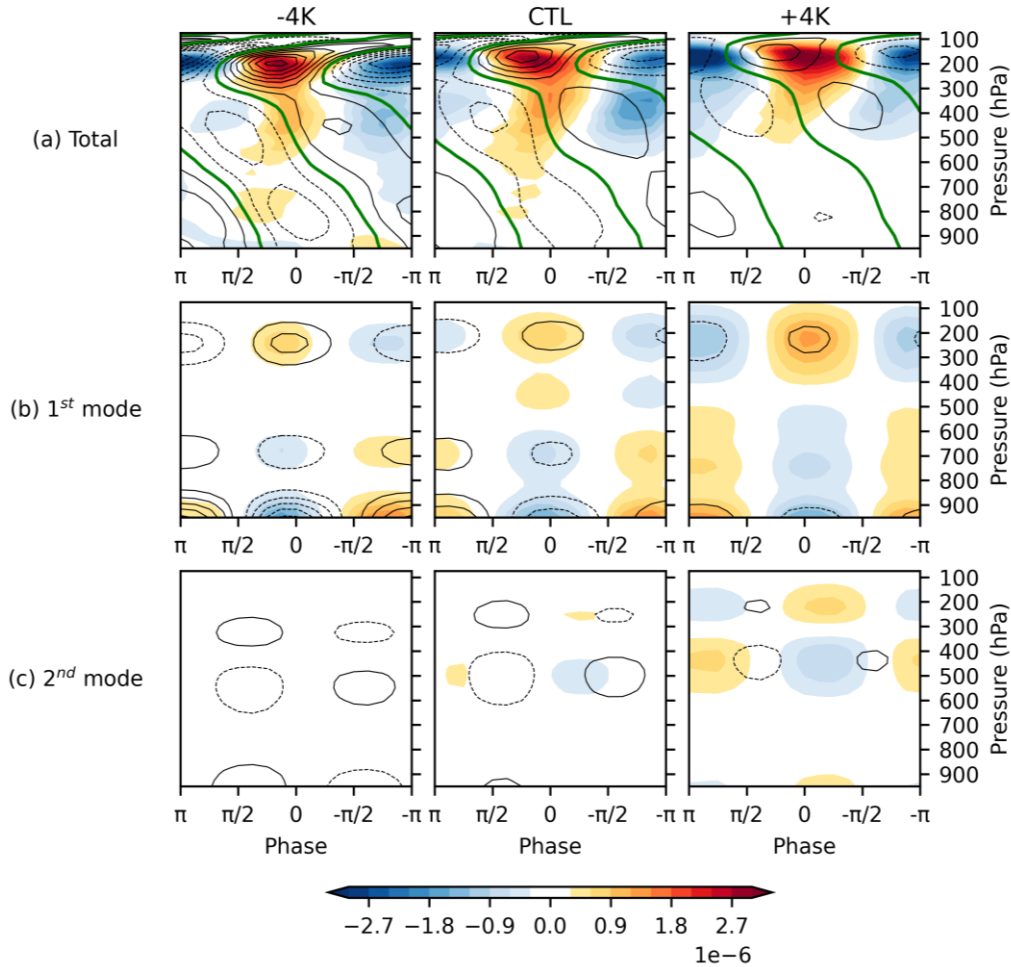
405 Figure 7b shows the KW composite diabatic heating and temperature anomalies of the
406 first baroclinic mode. The first mode heating minimizes at the most suppressed phase ($-\pi/2$) and
407 maximizes at the most enhanced phase ($+\pi/2$), consistent with the evolution of precipitation
408 anomalies. The temperature of the first mode is from in quadrature to slightly out of phase with
409 the first mode heating anomalies, meaning that warm anomalies overlap with cooling and the
410 cold anomalies overlap with heating, leading to a negative KW EAPE growth rate within the first
411 mode (Fig. 9). Figure 7c shows the heating and temperature anomalies of the second baroclinic
412 mode. The second mode heating anomalies with cooling aloft and heating below, indicating the
413 congestus processes, occur slightly after the most suppressed phase; the second mode heating
414 anomalies with heating aloft and cooling below, indicating the stratiform processes, slightly lag
415 the deep convective heating by about $\pi/8$ to $\pi/4$. Opposite to the negative correlation between
416 temperature and heating of the first mode, the second mode temperature anomalies are roughly in
417 phase with the second mode heating and cooling, with warm anomalies overlapping with heating
418 and cold anomalies overlapping with cooling. The positive correlation between temperature and
419 heating of the second mode would lead to a positive KW EAPE growth rate within the second
420 mode.

421 Figure 7b also shows that in a warmer climate, the first mode heating maximizes at a
422 lower pressure level (higher elevation) (also shown in Fig. 4a), indicating deep convection
423 deepens. Meanwhile, the out-of-phase relationship between the first mode heating and
424 temperature is more obvious in a warmer climate, suggesting that the damping of the KW EAPE
425 within the first mode structure is stronger. Figure 7c shows that in a warmer climate, the melting
426 level rises, and the second mode structure stretches upward (also shown in Fig. 6a). Meanwhile,
427 the lower tropospheric temperature anomalies near the boundary layer are weaker. In addition,
428 from -4K to +4K, the second mode heating and temperature anomalies become less in phase,
429 which suggests that the KW EAPE growth within the second mode decreases. As the surface

430 warms, the stronger KW EAPE damping of the first mode and the weaker KW EAPE growth
431 may lead to the weakening of KWs.

432 To investigate the change in KW amplitude, we may also need to consider the effect of
433 midlatitude forcing in KW maintenance. Figure 8a shows the KW composite vertical structure of
434 momentum flux convergence (shading) and zonal wind (contour) anomalies. Figure 8b shows
435 those of the first baroclinic mode. At the most suppressed phase ($-\pi/2$), the low-level zonal wind
436 divergence and the upper-level zonal wind convergence are the strongest, consistent with the
437 strongest first baroclinic cooling anomalies which are associated with the downward motion.
438 Oppositely, at the most enhanced phase ($+\pi/2$), the low-level zonal wind convergence and the
439 upper-level zonal wind divergence are the strongest, consistent with the strongest first baroclinic
440 heating anomalies which are associated with the upward motion. Figure 8c shows the momentum
441 flux convergence and zonal wind anomalies within the second baroclinic mode. The mid-level
442 zonal wind divergence, which is the signature of the circulation associated with congestus
443 clouds, occurs slightly after the most suppressed phase; the mid-level zonal wind convergence,
444 which is the signature of the circulation of stratiform processes, occurs slightly after the most
445 enhanced phase. The zonal wind structure in our simulations, as well as the thermodynamic
446 structure in Fig. 7, show robust evolution from suppressed convection, congestus, deep
447 convection, to stratiform processes within the life cycle of KWs, consistent with our
448 understanding of canonical KWs.

449



450
 451 **Figure 8.** Vertical mode decomposition of the KW phase composite zonal momentum flux
 452 convergence (shading) and zonal wind anomalies (contour) in each simulation: (a) the total
 453 anomalies, (b) the first baroclinic mode obtained from the blue lines in Fig. 6b, and (c) the
 454 second baroclinic mode obtained from the red lines in Fig. 6b. The green contour in (a) indicates
 455 the zero line for the zonal wind anomalies. Solid contours represent positive values and dashed
 456 contours represent negative values. The contour interval is 2 m/s.
 457

458 Figure 8a also shows that the momentum flux convergence maximizes at the upper levels
 459 near 200hPa, consistent with previous studies which showed that the extratropical influence on
 460 KWs originates from the upper troposphere (e.g., Straub and Kiladis 2003; Tulich and Kiladis
 461 2021; Cheng et al. 2022). In all simulations, the upper-level momentum flux convergence
 462 coexists with the maximum KW westerly, while the momentum flux divergence coexists with
 463 the maximum KW easterly, which would amplify the KW EKE, as mentioned in Section 1.
 464 Similar to the vertical mode decomposition of diabatic heating and temperature anomalies in Fig.
 465 7, the momentum flux convergence and zonal wind anomalies are also decomposed into the first

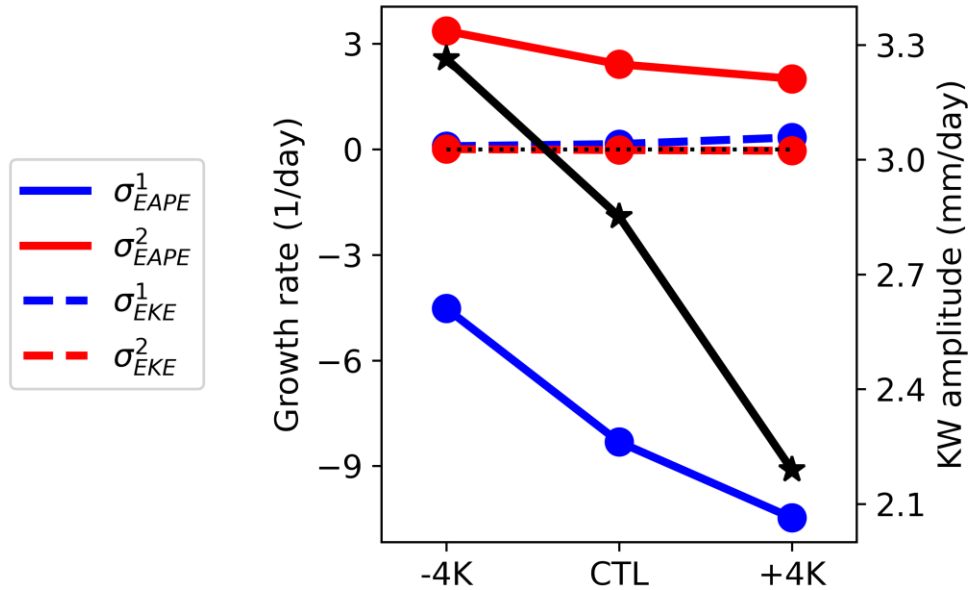
466 (Fig. 8b) and second (Fig. 8c) mode components. Figure 8b shows that the first mode zonal wind
467 and momentum flux convergence positively overlap with each other, contributing to positive
468 KW EKE growth rate of the first mode. Compared to the first mode, the second mode zonal wind
469 and momentum flux convergence is less positively overlapping and more in quadrature (Fig. 8c),
470 yielding a small KW EKE growth rate of the second mode.

471 From -4K to +4K, Figure 8b shows that the first mode zonal wind structure expands to
472 the upper troposphere (also shown in Fig. 6b), consistent with the expansion of the depth of deep
473 convection mentioned above (Fig. 7b). In terms of the magnitude changes from -4K to +4K,
474 Figure 8b shows that the zonal wind anomalies weaken, and the momentum flux divergence
475 anomalies strengthen. Stronger momentum flux divergence anomalies in a warmer climate may
476 come from stronger midlatitude wave activities, or stronger midlatitude-tropics interactions due
477 to the change in the basic state zonal wind, or both. In any case, our results suggest a larger KW
478 EKE growth rate within the first mode, which may amplify KWs in a warmer climate. Stronger
479 external forcing (Fig. 8) and weaker internal thermodynamic feedback (Fig. 7) in response to
480 surface warming may amplify and weaken KWs, respectively. The amplitude change would
481 depend on the relative magnitude of the KW EAPE and KW EKE growth rate.

482 To summarize the effect of internal thermodynamic feedback and external forcing on KW
483 growth, Figure 9 shows the KW EAPE and KW EKE growth rates of the two vertical modes. In
484 all simulations, the KW EKE growth rates, although positive, are roughly two orders of
485 magnitudes smaller than that of the KW EAPE growth rates. This suggests that internal
486 thermodynamic feedback is the dominant KW maintenance mechanism while the external
487 momentum forcing only plays a minimal role in our simulations. Furthermore, the KW EAPE
488 growth rate of the first mode (blue solid line) is negative and the KW EAPE growth rate of the
489 second mode (red solid line) is positive in all simulations, consistent with what was shown in
490 most reanalysis products (Chien and Kim 2023) and simple models which promote the
491 importance of stratiform and congestus processes in KW destabilization (e.g., Mapes 2000;
492 Khouider and Majda 2006; Kuang 2008).

493 From -4K to +4K, the KW EAPE growth of the second mode weakens while the KW
494 EAPE damping of the first mode strengthens (shown in solid lines in Fig. 9, consistent with Fig.
495 7b-c). Meanwhile, the KW EKE growth of the first mode slightly strengthens with warming
496 (shown in dashed lines in Fig. 9, consistent with Fig. 8b). To sum up, the weakening trend of

497 KW amplitude as the surface warms aligns with the decrease of KW EAPE growth of the first
 498 and second modes. This suggests that the weakening of KWs in a warmer climate is associated
 499 with the weakening of internal thermodynamic feedback, as opposed to the small increase of
 500 external forcing. However, it should be noted that the KW EAPE growth of the first or second
 501 mode alone cannot fully account for the weakening of KWs with surface warming.
 502

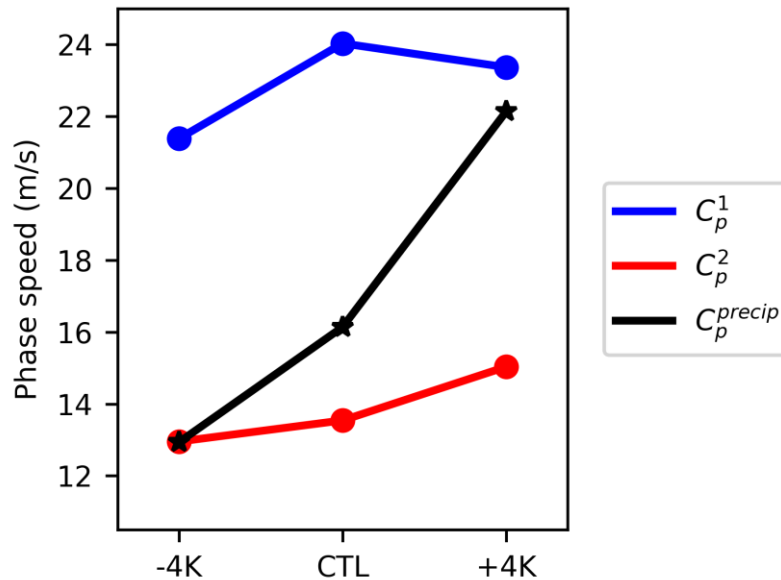


503 **Figure 9.** The growth rates of the KW EAPE (solid lines) and KW EKE (dashed lines) of the
 504 first and second modes in all simulations. The growth rates of the first mode are indicated in blue
 505 lines and those of the second mode are indicated in red lines. KW amplitude is indicated in
 506 black, with numbers showing on the y-axis on the right.
 507
 508

509 3.3. Causes of the changes in KW phase speed

510 Recall that we have shown that KWs accelerate with warming. To examine what factors
 511 determine the KW phase speed changes, we compare the apparent phase speed of KW
 512 convective signals with the theoretical phase speed of the two vertical modes (Fig. 10). While the
 513 apparent KW phase speed is estimated from the regression slope of KW precipitation in Fig. 4,
 514 the theoretical phase speeds of the two modes are calculated from Eqs. (10) and (11). The black
 515 line in Fig. 10a shows that the apparent KW phase speed increases from 12.94 m/s to 22.14 m/s
 516 from -4K to +4K (7.1 %/K). While KW phase speed may be affected by the mean barotropic
 517 zonal wind (Dias and Kiladis 2014), the increase in the mean barotropic zonal westerly by 2.9

518 m/s from -4K to +4K cannot fully explain the increase in KW phase speed by 9.2 m/s in our
 519 simulations. Therefore, the change in KW phase speed likely comes from the change in other
 520 factors (i.e. the terms in Eq. (11)). The theoretical KW phase speeds with the first or second
 521 baroclinic modes are shown in a blue and red line, respectively. The KWs with the first
 522 baroclinic structure propagate faster than the KWs with the second baroclinic structure. The
 523 phase speed of the KWs with the second baroclinic structure increases from 12.95 m/s to 15.03
 524 m/s from -4K to +4K (1.9 %/K) and the phase speed of the KWs with the first baroclinic
 525 structure increases from 21.39 m/s to 24.03 m/s from -4K to CTL (3.1 %/K). The increase in the
 526 first or second mode KW phase speed with warming is mostly due to the increase in tropospheric
 527 depth (dashed lines in Fig. S2 b-c). The first mode KW phase speed slightly decreases from CTL
 528 to +4K, due to stronger offset of adiabatic cooling by diabatic heating (larger α in Eq. (11))
 529 (dotted line in Fig. S2b), which overcomes the effect of increased tropospheric depth.
 530 Nevertheless, considering the changes in the KW phase speed of the first or second mode alone
 531 cannot fully account for the changes in the apparent KW phase speed. In fact, the apparent KW
 532 phase speed is closer to the second mode KW phase speed in -4K, whereas it is closer to the first
 533 mode KW phase speed in +4K.
 534

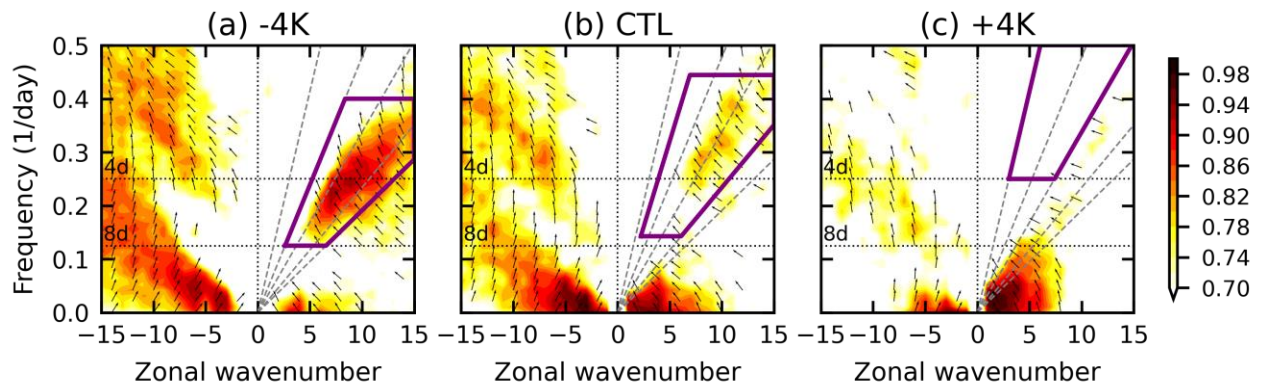


535 **Figure 10.** KW apparent phase speed (black, obtained from the regression slope in Fig. 4) and
 536 the theoretical KW phase speed for the first (blue) and second (red) modes (obtained from Eq.
 537 (10) and Eq. (11)) in all simulations.
 538
 539

540 3.4. Synthesis

541 Both the weakening and acceleration of KWs in response to surface warming cannot be
 542 solely explained by the changes in a single vertical mode, in terms of the KW EAPE growth
 543 (Fig. 9) or the estimated phase speed (Fig. 10). Specifically, KWs propagate slower at phase
 544 speed closer to that of the second mode KW in -4K, whereas in +4K, KWs propagate faster at
 545 phase speed closer to that of the first mode KW (Fig. 10). Meanwhile, stronger KWs in -4K may
 546 be due to the growth of the second mode via positive KW EAPE generation, while weaker KWs
 547 in +4K may be associated with the damping of the first mode via negative KW EAPE generation
 548 (Fig. 9). To investigate the coupling between the two modes, Figure 11 shows the coherence
 549 squared between the first and second mode heating in wavenumber-frequency space. Within the
 550 KW band, the first mode heating is strongly coupled with the second mode heating in -4K, while
 551 the two modes are weakly coupled in +4K.

552



553

554 **Figure 11.** The coherence squared (shading) and phase relationship (arrows) between the first
 555 and second principal components of diabatic heating. Arrows pointing leftward (rightward)
 556 represent the second mode lagging (leading) the first mode; arrows pointing upward (downward)
 557 represent the second mode in phase (out of phase) with the first mode. KW band is indicated in
 558 purple polygons.
 559

560 Synthesizing the results presented in Figs. 9, 10, and 11, we hypothesize that in -4K,
 561 when the first and second modes are strongly coupled, KWs destabilize through positive
 562 feedback between the second mode heating and temperature. This positive feedback would lead
 563 to stronger KWs (i.e., stronger temperature, zonal wind, and precipitation anomalies).
 564 Meanwhile, since KWs destabilize within the second mode component, their propagation speed
 565 also follows the second mode KW phase speed, which is determined by the adiabatic heating and
 566 cooling rate associated with the second baroclinic vertical motion. In +4K, as the first and second

567 modes are weakly coupled, KWs are less affected by the second modes, and thus they are
568 dominated by the first mode. The first mode heating is negatively correlated with the first mode
569 temperature variability, producing a negative KW EAPE growth rate. This negative feedback
570 would lead to weaker KWs (i.e., weaker temperature, zonal wind, and precipitation anomalies).
571 Meanwhile, since the first baroclinic mode dominates KWs, the propagation speed of the KWs is
572 faster, as it follows the first mode KW phase speed. This faster first mode phase speed is due to a
573 stronger adiabatic cooling and heating associated with the first baroclinic vertical motion than
574 those of the second baroclinic motion.

575 **4 Summary and Conclusions**

576 This study investigated the changes in KW characteristics in response to surface warming
577 and explored their causes. We conducted a set of three aquaplanet simulations by prescribing
578 zonally uniform and meridionally varying sea surface temperatures (SST) boundary conditions.
579 For the control simulation, a profile based on the observed SST distribution is used (Neale and
580 Hoskins 2000). For warmer and cooler climates, we added and subtracted 4K uniformly over the
581 entire globe (+4K and -4K, respectively). The simulation results showed that KWs weakened
582 and accelerated as the surface warms. The eddy available potential energy (EAPE) and eddy
583 kinetic energy (EKE) budget of the KWs suggested that KWs in the simulations were mainly
584 maintained by the internal thermodynamic feedback. We found that the weakening of KWs was
585 associated with (1) a weakening of positive EAPE generation within the second baroclinic mode
586 and (2) a strengthening of negative EAPE generation within the first baroclinic mode. In
587 addition, the KW phase speed diagnostics showed that KWs' phase speed in -4K (~12.94 m/s) is
588 close to the theoretical second mode KW phase speed, while their phase speed in +4K (~22.14
589 m/s) is close to the theoretical first mode KW phase speed. We also found that the first and
590 second modes were strongly coupled within KWs in -4K, while they are weakly coupled in +4K.

591 Synthesizing our results, we hypothesized that the KWs weakened and accelerated with
592 warming because different dynamics dominated KWs' propagation and maintenance. In -4K,
593 KWs destabilize through positive feedback between the second mode heating and temperature,
594 which is possible because the first and second baroclinic modes are strongly coupled. This
595 positive feedback would lead to stronger KWs (i.e., stronger temperature, zonal wind, and
596 precipitation anomalies). Meanwhile, since KWs destabilize within the second mode component,

597 their propagation speed follows the theoretical second mode KW phase speed. In +4K, as the
598 coupling between the first and second modes weakens, KWs dynamics appear to be dominated
599 by that of the first baroclinic mode KWs. Because the first mode heating is negatively correlated
600 with the first mode temperature variability, producing a negative EAPE growth rate, KWs in
601 +4K are damped and hence exhibit weaker variability (i.e., weaker temperature, zonal wind, and
602 precipitation anomalies). Meanwhile, since the first baroclinic mode dynamics dominates, the
603 propagation speed of KWs follows that of the theoretical first mode KW phase speed.

604 Our results suggest that the mean state changes have substantial impacts on the amplitude
605 and phase speed of KWs. One of the remaining important questions is why the coupling between
606 the two vertical modes weakens in a warmer climate. An in-depth study of the coupling
607 mechanism is warranted, which should also examine whether our simulation results can be
608 explained by any of the previously proposed coupling mechanisms (e.g., Mapes 2000; Khouider
609 and Majda 2006; Kuang 2008).

610 It is worth noting that our results contradict to that of Bartana et al. (2022), who found that
611 KWs intensify in a warmer climate in CMIP6 models. A possible reason for the discrepancy is
612 the difference in the mean state temperature changes. While we use zonally uniform and
613 meridionally symmetric SST profiles, the SST changes in CMIP6 model simulations have strong
614 zonal and meridional asymmetry. To what extent the SST asymmetry affects the changes of
615 KWs is not clear. Future studies can use more realistic SST warming and cooling patterns to
616 investigate the extent to which zonal and meridional asymmetry of SST changes affect KW
617 characteristics.

618

619 **Acknowledgments**

620 The aquaplanet simulations were performed based on high-performance computing
621 resources from Cheyenne (doi:10.5065/D6RX99HX) and Derecho (doi: 10.5065/qx9a-pg09)
622 provided by NCAR's Computational and Information Systems Laboratory, sponsored by the
623 National Science Foundation. MC was supported by PhD Fellowship from Taiwanese Ministry
624 of Science and Technology. DK was supported by New Faculty Startup Fund from Seoul
625 National University, NASA MAP program (80NSSC21K1495), NOAA MAPP program
626 (NA21OAR4310343), and NOAA CVP program (NA22OAR4310608).

627

628 **Open Research**

629 The aquaplanet simulation outputs and the codes for analysis are uploaded on Github
630 with the following link: https://github.com/muting-chien/CCKW_aquaplanet. The analysis codes
631 are written mostly in functions, and therefore they can be easily applied to analyze KWs in
632 observations and other model simulations.

633

634 **References**

635

636 Adames, Á. F., D. Kim, A. H. Sobel, A. Del Genio, and J. Wu, 2017a: Changes in the structure
637 and propagation of the MJO with increasing CO₂. *J. Adv. Model. Earth Syst.*, 9, 1251–1268,
638 <https://doi.org/10.1002/2017MS000913>

639

640 Adames, Á. F., D. Kim, A. H. Sobel, A. Del Genio, and J. Wu, 2017b: Characterization of Moist
641 Processes Associated With Changes in the Propagation of the MJO With Increasing CO₂. *J.*
642 *Adv. Model. Earth Syst.*, 9, 2946–2967, <https://doi.org/10.1002/2017MS001040>

643

644 Bartana, H., Garfinkel, C. I., Shamir, O., & Rao, J. (2022). Projected future changes in equatorial
645 wave spectrum in CMIP6. *Climate Dynamics*, 1-13, <https://doi.org/10.1007/s00382-022-06510-y>

646

647 Bessafi, M., and M. C. Wheeler, 2006: Modulation of south Indian Ocean tropical cyclones by
648 the Madden–Julian oscillation and convectively coupled equatorial waves. *Mon. Wea. Rev.*, 134,
649 638–656, <https://doi.org/10.1175/MWR3087.1>.

650

651 Bogenschutz, P. A., Gettelman, A., Morrison, H., Larson, V. E., Craig, C., & Schanen, D. P.
652 (2013). Higher-order turbulence closure and its impact on climate simulations in the Community
653 Atmosphere Model. *Journal of Climate*, 26(23), 9655–9676, [https://doi.org/10.1175/JCLI-D-13-](https://doi.org/10.1175/JCLI-D-13-00075.1)
654 [00075.1](https://doi.org/10.1175/JCLI-D-13-00075.1)

655

656 Bui, H. X., and E. D. Maloney, 2020: Changes to the Madden-Julian Oscillation in Coupled and
657 Uncoupled Aquaplanet Simulations With 4xCO₂. *J. Adv. Model. Earth Syst.*, 12,
658 e2020MS0021799, <https://doi.org/10.1029/2020MS002179>

659
660
661
662
663
664
665
666
667
668
669
670
671
672
673
674
675
676
677
678
679
680
681
682
683
684
685
686
687
688

Chen, W. T., Hsu, S. P., Tsai, Y. H., & Sui, C. H. (2019). The influences of convectively coupled Kelvin waves on multiscale rainfall variability over the South China Sea and Maritime Continent in December 2016. *Journal of Climate*, 32(20), 6977-6993, <https://doi.org/10.1175/JCLI-D-18-0471.1>

Cheng, Y. M., Tulich, S., Kiladis, G. N., & Dias, J. (2022). Two extratropical pathways to forcing tropical convective disturbances. *Journal of Climate*, 35(20), 2987-3009, <https://doi.org/10.1175/JCLI-D-22-0171.1>

Cheng, Y. M., Dias, J., Kiladis, G., Feng, Z., & Leung, L. R. (2023). Mesoscale convective systems modulated by convectively coupled equatorial waves. *Geophysical Research Letters*, 50(10), e2023GL103335. <https://doi.org/10.1029/2023GL103335>

Chien, M. T., & Kim, D. (2023). Representation of the Convectively Coupled Kelvin Waves in Modern Reanalysis Products. *Journal of the Atmospheric Sciences*, 80(2), 397-418, <https://doi.org/10.1175/JAS-D-22-0067.1>

Computational and Information Systems Laboratory. (2019). Cheyenne: HPE/SGI ICE XA System (University Community Computing). Boulder, CO: National Center for Atmospheric Research. <https://doi.org/10.5065/D6RX99HX>.

Computational and Information Systems Laboratory. (2024). Derecho: HPE Cray EX System (University Community Computing). Boulder, CO: National Center for Atmospheric Research. <https://doi.org/10.5065/qx9a-pg09>.

Dias, J., & Pauluis, O. (2011). Modulations of the phase speed of convectively coupled Kelvin waves by the ITCZ. *Journal of the atmospheric sciences*, 68(7), 1446-1459, <https://doi.org/10.1175/2011JAS3630.1>

- 689 Dias, J., & Kiladis, G. N. (2014). Influence of the basic state zonal flow on convectively coupled
690 equatorial waves. *Geophysical Research Letters*, *41*(19), 6904-6913,
691 <https://doi.org/10.1002/2014GL061476>
692
- 693 Emanuel, K. A., 1987: An air–sea interaction model of intraseasonal oscillations in the tropics. *J.*
694 *Atmos. Sci.*, *44*, 2324–2340, [https://doi.org/10.1175/1520-](https://doi.org/10.1175/1520-0469(1987)044,2324:AASIMO.2.0.CO;2)
695 [0469\(1987\)044,2324:AASIMO.2.0.CO;2](https://doi.org/10.1175/1520-0469(1987)044,2324:AASIMO.2.0.CO;2).
696
- 697 Flatau, M. K., P. J. Flatau, J. Schmidt, and G. N. Kiladis, 2003: Delayed onset of the 2002 Indian
698 monsoon. *Geophys. Res. Lett.*, *30*, 1768, <https://doi.org/10.1029/2003GL017434>.
699
- 700 Gettelman, A., & Morrison, H. (2015). Advanced two-moment bulk microphysics for global
701 models. Part I: Off-line tests and comparison with other schemes. *Journal of Climate*, *28*(3),
702 1268-1287, <https://doi.org/10.1175/JCLI-D-14-00102.1>
703
704
- 705 Golaz, J. C., Larson, V. E., & Cotton, W. R. (2002). A PDF-based model for boundary layer
706 clouds. Part I: Method and model description. *Journal of the atmospheric sciences*, *59*(24), 3540-
707 3551, [https://doi.org/10.1175/1520-0469\(2002\)059<3540:APBMFB>2.0.CO;2](https://doi.org/10.1175/1520-0469(2002)059<3540:APBMFB>2.0.CO;2)
708
- 709 Hoskins, B. J., & Yang, G. Y. (2000). The equatorial response to higher-latitude forcing. *Journal*
710 *of the atmospheric sciences*, *57*(9), 1197-1213, [https://doi.org/10.1175/1520-](https://doi.org/10.1175/1520-0469(2000)057<1197:TERTHL>2.0.CO;2)
711 [0469\(2000\)057<1197:TERTHL>2.0.CO;2](https://doi.org/10.1175/1520-0469(2000)057<1197:TERTHL>2.0.CO;2)
712
- 713 Iacono, M. J., Delamere, J. S., Mlawer, E. J., Shephard, M. W., Clough, S. A., & Collins, W. D.
714 (2008). Radiative forcing by long-lived greenhouse gases: Calculations with the AER radiative
715 transfer models. *Journal of Geophysical Research: Atmospheres*, *113*(D13),
716 <https://doi.org/10.1029/2008JD009944>
717

- 718 Kiladis, G. N., Wheeler, M. C., Haertel, P. T., Straub, K. H., & Roundy, P. E. (2009).
719 Convectively coupled equatorial waves. *Reviews of Geophysics*, 47(2),
720 <https://doi.org/10.1029/2008RG000266>
721
- 722 Khouider, B., & Majda, A. J. (2006). A simple multicloud parameterization for convectively
723 coupled tropical waves. Part I: Linear analysis. *Journal of the atmospheric sciences*, 63(4), 1308-
724 1323, <https://doi.org/10.1175/JAS3677.1>
725
- 726 Kuang, Z., 2008: A moisture-stratiform instability for convectively coupled waves. *J. Atmos.*
727 *Sci.*, 65, 834–854, <https://doi.org/10.1175/2007JAS2444.1>.
728
- 729 Lawton, Q. A., & Majumdar, S. J. (2023). Convectively Coupled Kelvin Waves and Tropical
730 Cyclogenesis: Connections through Convection and Moisture. *Monthly weather review*, 151(7),
731 1647-1666, <https://doi.org/10.1175/MWR-D-23-0005.1>
732
- 733 Latos, B., and Coauthors, 2021: Equatorial waves triggering extreme rainfall and floods in
734 southwest Sulawesi, Indonesia. *Mon. Wea. Rev.*, 149, 1381–1401,
735 <https://doi.org/10.1175/MWRD-20-0262.1>.
736
- 737 Leroux, S., Bellon, G., Roehrig, R., Caian, M., Klingaman, N. P., Lafore, J. P., ... & Tyteca, S.
738 (2016). Inter-model comparison of subseasonal tropical variability in aquaplanet experiments:
739 Effect of a warm pool. *Journal of Advances in Modeling Earth Systems*, 8(4), 1526-1551,
740 <https://doi.org/10.1002/2016MS000683>
741
- 742 Lin, S. J. (2004). A “vertically Lagrangian” finite-volume dynamical core for global
743 models. *Monthly Weather Review*, 132(10), 2293-2307, [https://doi.org/10.1175/1520-0493\(2004\)132<2293:AVLFDC>2.0.CO;2](https://doi.org/10.1175/1520-0493(2004)132<2293:AVLFDC>2.0.CO;2)
744
- 745
- 746 Lindzen, R. S., 1974: Wave-CISK in the tropics. *J. Atmos. Sci.*, 31, 156–179,
747 [https://doi.org/10.1175/1520-0469\(1974\)031,0156:WCITT.2.0.CO;2](https://doi.org/10.1175/1520-0469(1974)031,0156:WCITT.2.0.CO;2).
748

- 749 Mapes, B. E., 2000: Convective inhibition, subgrid-scale triggering energy, and stratiform
750 instability in a toy tropical wave model. *J. Atmos. Sci.*, 57, 1515–1535,
751 [https://doi.org/10.1175/1520-469\(2000\)057,1515:CISSTE.2.0.CO;2](https://doi.org/10.1175/1520-469(2000)057,1515:CISSTE.2.0.CO;2).
- 752
- 753 Murata, F., M. D. Yamanaka, H. Hashiguchi, S. Mori, M. Kudsy, T. Sribimawati, B. Suhardi,
754 and Emrizal, 2006: Dry intrusions following eastward-propagating synoptic-scale cloud systems
755 over Sumatera Island. *J. Meteor. Soc. Japan*, 84, 277–294, <https://doi.org/10.2151/jmsj.84.277>.
- 756
- 757 Nakamura, Y., & Takayabu, Y. N. (2022). Convective Couplings with Equatorial Rossby Waves
758 and Equatorial Kelvin Waves. Part I: Coupled Wave Structures. *Journal of the Atmospheric*
759 *Sciences*, 79(1), 247-262, <https://doi.org/10.1175/JAS-D-21-0080.1>
- 760
- 761 Neale, R. B., & Hoskins, B. J. (2000). A standard test for AGCMs including their physical
762 parametrizations: I: The proposal. *Atmospheric Science Letters*, 1(2), 101-107,
763 <https://doi.org/10.1006/asle.2000.0019>
- 764
- 765 Randel, W., & Held, I. (1991). Phase speed spectra of transient eddy fluxes and critical layer
766 absorption. *Journal of the atmospheric sciences*, 48(5), 688-697, [https://doi.org/10.1175/1520-0469\(1991\)048<0688:PSSOTE>2.0.CO;2](https://doi.org/10.1175/1520-0469(1991)048<0688:PSSOTE>2.0.CO;2)
- 767
- 768
- 769 Raymond, D. J., and Z^ˆ. Fuchs, 2007: Convectively coupled gravity and moisture modes in a
770 simple atmospheric model. *Tellus*, 59A, 627–640, <https://doi.org/10.1111/j.1600-0870.2007.00268.x>.
- 771
- 772
- 773 Rios-Berrios, R., Judt, F., Bryan, G., Medeiros, B., & Wang, W. (2023). Three-Dimensional
774 Structure of Convectively Coupled Equatorial Waves in Aquaplanet Experiments with Resolved
775 or Parameterized Convection. *Journal of Climate*, 1-44, <https://doi.org/10.1175/JCLI-D-22-0422.1>
- 776
- 777
- 778 Roundy, P. E., 2008: Analysis of convectively coupled Kelvin waves in the Indian Ocean MJO.
779 *J. Atmos. Sci.*, 65, 1342–1359, <https://doi.org/10.1175/2007JAS2345.1>.

780

781 Roundy, P. E. and W. M. Frank, 2004: A climatology of waves in the equatorial region. *J.*
782 *Atmos. Sci.*, 61, 2105–2132, [https://doi.org/10.1175/1520-](https://doi.org/10.1175/1520-0469(2004)061,2105:ACOWIT.2.0.CO;2)
783 [0469\(2004\)061,2105:ACOWIT.2.0.CO;2](https://doi.org/10.1175/1520-0469(2004)061,2105:ACOWIT.2.0.CO;2).

784

785 Rushley, S. S., Kim, D., & Adames, Á. F. (2019). Changes in the MJO under greenhouse gas–
786 induced warming in CMIP5 models. *Journal of Climate*, 32(3), 803–821,
787 <https://doi.org/10.1175/JCLI-D-18-0437.1>

788

789 Sinclair, Z., A. Lenouo, C. Tchawoua, and S. Janicot, 2015: Synoptic Kelvin type perturbation
790 waves over Congo basin over the period 1979–2010. *J. Atmos. Sol.-Terr. Phys.*, 130–131, 43–56,
791 <https://doi.org/10.1016/j.jastp.2015.04.015>.

792

793 Straub, K. H., and G. N. Kiladis, 2002: Observations of a convectively coupled Kelvin wave in
794 the eastern Pacific ITCZ. *J. Atmos. Sci.*, 59, 30–53, [https://doi.org/10.1175/1520-0469\(2002\)](https://doi.org/10.1175/1520-0469(2002)059,0030:OOACCK.2.0.CO;2)
795 [059,0030:OOACCK.2.0.CO;2](https://doi.org/10.1175/1520-0469(2002)059,0030:OOACCK.2.0.CO;2).

796

797 Straub, K. H, G. N. Kiladis, 2003a: The observed structure of convectively coupled Kelvin
798 waves: Comparison with simple models of coupled wave instability. *J. Atmos. Sci.*, 60, 1655–
799 1668, [https://doi.org/10.1175/1520-0469\(2003\)060,1655:TOSOCC.2.0.CO;2](https://doi.org/10.1175/1520-0469(2003)060,1655:TOSOCC.2.0.CO;2).

800

801 Straub, K. H., & Kiladis, G. N, 2003b. Extratropical forcing of convectively coupled Kelvin
802 waves during austral winter. *Journal of the atmospheric sciences*, 60(3), 526–543,
803 [https://doi.org/10.1175/1520-0469\(2003\)060<0526:EFOCCK>2.0.CO;2](https://doi.org/10.1175/1520-0469(2003)060<0526:EFOCCK>2.0.CO;2)

804

805 Straub, K. H., G. N. Kiladis, and P. E. Ciesielski, 2006: The role of equatorial waves in the onset
806 of the South China Sea summer monsoon and the demise of El Niño during 1998. *Dyn. Atmos.*
807 *Oceans*, 42, 216–238, <https://doi.org/10.1016/j.dynatmoce.2006.02.005>.

808

809 Tulich, S. N., & Kiladis, G. N. (2021). On the regionality of moist Kelvin waves and the MJO:
810 The critical role of the background zonal flow. *Journal of Advances in Modeling Earth Systems*,
811 *13*(9), e2021MS002528, <https://doi.org/10.1029/2021MS002528>

812

813 Wang, H., and R. Fu, 2007: The influence of Amazon rainfall on the Atlantic ITCZ through
814 convectively coupled Kelvin waves. *J. Climate*, *20*, 1188–1201,
815 <https://doi.org/10.1175/JCLI4061.1>.

816

817 Wang, L., and L. Chen, 2016: Interannual variation of convectively coupled equatorial waves
818 and their association with environmental factors. *Dyn. Atmos. Oceans*, *76*, 116–126,
819 <https://doi.org/10.1016/j.dynatmoce.2016.10.004>.

820

821 Weber, Nicholas J., Daehyun Kim, and Clifford F. Mass. "Convection–Kelvin wave coupling in
822 a global convection-permitting model." *Journal of the Atmospheric Sciences* *78.4* (2021): 1039-
823 1055, <https://doi.org/10.1175/JAS-D-20-0243.1>

824

825 Wheeler, M., and G. N. Kiladis, 1999: Convectively coupled equatorial waves: Analysis of
826 clouds and temperature in the wavenumber–frequency domain. *J. Atmos. Sci.*, *56*, 374–399,
827 [https://doi.org/10.1175/1520-0469\(1999\)056,0374:CCEWAO.2.0.CO;2](https://doi.org/10.1175/1520-0469(1999)056<0374:CCEWAO.2.0.CO;2).

828

829 Yang, G. Y., Hoskins, B., & Slingo, J. (2007). Convectively coupled equatorial waves. Part I:
830 Horizontal and vertical structures. *Journal of the atmospheric sciences*, *64*(10), 3406-3423,
831 <https://doi.org/10.1175/JAS4017.1>

832

833 Yasunaga, K., 2011: Seasonality and regionality of the Madden-Julian oscillation and
834 convectively coupled equatorial waves. *SOLA*, *7*, 153–156, <https://doi.org/10.2151/sola.2011-039>.

835

836
837 Zhang, G. J., & McFarlane, N. A. (1995). Role of convective scale momentum transport in
838 climate simulation. *Journal of Geophysical Research: Atmospheres*, *100*(D1), 1417-1426,
839 <https://doi.org/10.1029/94JD02519>